Hindawi Publishing Corporation
Computational and Mathematical Methods in Medicine
Volume 2013, Article ID 398042, 12 pages
http://dx.doi.org/10.1155/2013/398042

Research Article

Effectiveness of Variable-Gain Kalman Filter Based on Angle Error Calculated from Acceleration Signals in Lower Limb Angle Measurement with Inertial Sensors

Yuta Teruyama and Takashi Watanabe

Graduate School of Biomedical Engineering, Tohoku University, Sendai 980-8579, Japan

Correspondence should be addressed to Yuta Teruyama; yuta.teruyama@bme.tohoku.ac.jp

Received 30 July 2013; Accepted 11 September 2013

Academic Editor: Imre Cikajlo

Copyright © 2013 Y. Teruyama and T. Watanabe. This is an open access article distributed under the Creative Commons Attribution License, which permits unrestricted use, distribution, and reproduction in any medium, provided the original work is properly cited.

The wearable sensor system developed by our group, which measured lower limb angles using Kalman-filtering-based method, was suggested to be useful in evaluation of gait function for rehabilitation support. However, it was expected to reduce variations of measurement errors. In this paper, a variable-Kalman-gain method based on angle error that was calculated from acceleration signals was proposed to improve measurement accuracy. The proposed method was tested comparing to fixed-gain Kalman filter and a variable-Kalman-gain method that was based on acceleration magnitude used in previous studies. First, in angle measurement in treadmill walking, the proposed method measured lower limb angles with the highest measurement accuracy and improved significantly foot inclination angle measurement, while it improved slightly shank and thigh inclination angles. The variable-gain method based on acceleration magnitude was not effective for our Kalman filter system. Then, in angle measurement of a rigid body model, it was shown that the proposed method had measurement accuracy similar to or higher than results seen in other studies that used markers of camera-based motion measurement system fixing on a rigid plate together with a sensor or on the sensor directly. The proposed method was found to be effective in angle measurement with inertial sensors.

1. Introduction

Wearable inertial sensors have been used in many studies to estimate human kinetic data. Those sensors have advantages of low cost, small size, and practical usefulness compared to traditional lab tools such as optical motion measurement system or electric goniometers. As has been reported in previous studies, segment and joint angles [1–11], stride length [1, 3, 5], walking speed [1, 5], gait event timing [5, 12, 13], and so on can be estimated using inertial sensors. Therefore, a wearable inertial sensor system can be effective for objective and quantitative evaluation in rehabilitation of motor function. That is, inertial sensors are considered to be suitable for clinical applications.

In our previous studies, a method of measuring lower limb angles using wireless inertial sensors was developed to realize simplified wearable gait evaluation system for rehabilitation support. The method was tested in measurement of gait of healthy subjects [14, 15]. Although the method was shown to have practical accuracy, measurement errors varied depending on movement speeds or subjects. In the angle measurement method of our previous studies, Kalman filter was applied using angle calculated from acceleration signals. Many other studies also used accelerometers as inclinometers to measure inclination angles of body segments [2, 5, 7, 8]. However, the angle calculated from acceleration signals was influenced by impact and movement accelerations, since the angle was calculated from gravitational acceleration. Therefore, those impact and movement accelerations can be considered as one of the causes of variation of measurement error.

Low-pass filtering of acceleration signals is one of the methods to reduce influences of those impact and motion accelerations. In our previous studies, outputs of accelerometer were filtered with Butterworth low-pass filter with cutoff frequency of 0.5 Hz [14, 15]. However, low cutoff frequency is at risk for increasing measurement error because of its large time constant in the low-pass filtering. Therefore,

using higher cutoff frequency has a possibility to improve measurement error.

In this paper, in order to reduce influences of impact and movement accelerations in calculation of angles using Kalman filter, a variable-Kalman-gain method with higher cutoff frequency for the low-pass filtering was tested. In previous studies, a method to change Kalman gain based on the magnitude of acceleration signals was used [9, 16]. However, in this study, the method to change Kalman gain based on error of angle calculated from acceleration signals was proposed. This is because the Kalman filter of our system is applied using the angles calculated from acceleration signals.

The variable-gain method was evaluated in measurement of lower limb angles of healthy subjects in treadmill walking using a camera-based motion measurement system to measure reference angles for evaluation. The fixed-Kalman-gain method and the variable-gain method based on magnitude of acceleration signals were compared to the proposed method. Then, similar evaluation was performed in measurement of angles of a rigid body model, because some other studies evaluated angle measurement method with inertial sensors using a rigid plate that fixed a sensor together with markers of an optical motion measurement system or attaching the markers directly on the sensor [4, 8, 10, 11].

2. Angle Measurement Method Based on Kalman Filter

2.1. Fixed-Kalman-Gain Method. Figure 1(a) shows the block diagram of the angle measurement method used in our previous studies. An inclination angle of body segment is calculated by integrating an output of a gyroscope. Here, the integration error is corrected by Kalman filter using the angle calculated from outputs of an accelerometer. Then, joint angle is calculated from difference of inclination angles of the adjacent segments.

The state equation is represented by error of angle measured with a gyroscope $\Delta\theta$ and bias offset of outputs of the gyroscope Δb as follows:

$$\begin{bmatrix} \Delta\theta_{k+1} \\ \Delta b_{k+1} \end{bmatrix} = \begin{bmatrix} 1 & \Delta t \\ 0 & 1 \end{bmatrix} \begin{bmatrix} \Delta\theta_k \\ \Delta b_k \end{bmatrix} + \begin{bmatrix} \Delta t \\ 1 \end{bmatrix} w, \tag{1}$$

where w is error in measurement with the gyroscope and Δt is sampling period. Observation signal is deference of angles obtained from the gyroscope and an accelerometer Δy, which is given by

$$\Delta y_k = \begin{bmatrix} 1 & 0 \end{bmatrix} \begin{bmatrix} \Delta\theta_k \\ \Delta b_k \end{bmatrix} + v, \tag{2}$$

where v is error in measurement with the accelerometer. On this state-space model, Kalman filter repeats corrections (3) and predictions (4):

$$\begin{bmatrix} \Delta\widehat{\theta}_k \\ \Delta\widehat{b}_k \end{bmatrix} = \begin{bmatrix} \Delta\widehat{\theta}_k^- \\ \Delta\widehat{b}_k^- \end{bmatrix} + \begin{bmatrix} K_1 \\ K_2 \end{bmatrix} \left(\Delta y_k - \Delta\widehat{\theta}_k^-\right), \tag{3}$$

$$\begin{bmatrix} \Delta\widehat{\theta}_{k+1}^- \\ \Delta\widehat{b}_{k+1}^- \end{bmatrix} = \begin{bmatrix} 1 & \Delta t \\ 0 & 1 \end{bmatrix} \begin{bmatrix} \Delta\widehat{\theta}_k \\ \Delta\widehat{b}_k \end{bmatrix}, \tag{4}$$

where K_1 and K_2 represent Kalman gain for $\Delta\theta$ and Δb, respectively. Notations such as $\Delta\widehat{\theta}$ and $\Delta\widehat{\theta}^-$ represent estimated value and predicted value for $\Delta\theta$, respectively. For the initial condition, $\Delta\widehat{\theta}_0^-$ was set as 0, and $\Delta\widehat{b}_0^-$ was set as $\Delta\widehat{b}$ at the last measurement. The Kalman filter was applied repeatedly until its output converged.

Values of Kalman gain were fixed in angle calculation in our previous studies. Those gain values are determined by the noise ratio, that is, the ratio of the covariance of observation noise and covariance of process noise. In our system, value of Kalman gain increases as the noise ratio decreases and decreases as the noise ratio increases.

As shown in (3) and (4), the Kalman filter estimates $\Delta\theta$ and Δb by using the angle difference Δy. Therefore, large value of Kalman gain (small noise ratio) means that calculation results become highly dependent on accelerometer, while small Kalman gain (large noise ratio) means that calculation results become highly dependent on gyroscope. Considering power of the correction by Kalman filter, values of the noise ratio were determined by trial and error method.

2.2. Variable-Kalman-Gain Method. The fixed-Kalman-gain method shown in the previous section was found to be useful in measurement of angles during gait of healthy subjects [14, 15]. However, impact and movement accelerations were considered to increase measurement error and its variation. That is, those accelerations are considered to cause inappropriate correction by the Kalman filter. As described in the previous section, Kalman gain means correction power of the Kalman filter. Therefore, in this paper, following two methods of changing the noise ratio to determine Kalman gain were tested.

(a) *Acceleration Magnitude-Based Method.* Figure 1(b) shows the variable-gain method based on acceleration magnitude, which was introduced in reference to previous studies [9, 16]. Value of the noise ratio is adjusted based on the magnitude of impact and motion acceleration signals. Here, the magnitude of impact and motion acceleration signals was calculated by subtracting gravitational acceleration (1 G) from magnitude of measured acceleration vector. That is, the value of noise ratio is varied as follows:

$$\begin{aligned} n &= n_1, \quad \text{for } |\alpha| \le \alpha_1, \\ n &= n_2, \quad \text{for } \alpha_1 < |\alpha| \le \alpha_2, \\ n &= n_3, \quad \text{for } \alpha_2 < |\alpha| \le \alpha_3, \\ n &= n_4, \quad \text{for } \alpha_3 < |\alpha|, \end{aligned} \tag{5}$$

where n and $|\alpha|$ represent the noise ratio and the magnitude of impact and motion acceleration signals, respectively. α_1, α_2, and α_3 show thresholds to change the value of noise ratio, respectively.

(b) *Angle Error-Based Method.* Figure 1(c) shows the method proposed in this paper, in which the noise ratio is adjusted based on the difference between the angle estimated by the Kalman filter and the angle calculated from acceleration signals. Here, the angle difference was used approximately as the

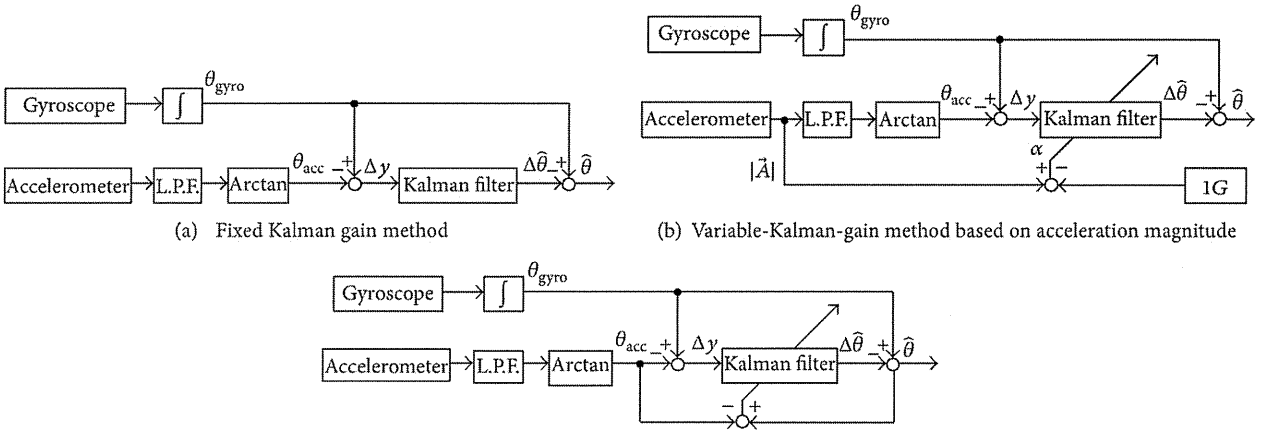

(a) Fixed Kalman gain method

(b) Variable-Kalman-gain method based on acceleration magnitude

(c) Variable-Kalman-gain method based on angle error

FIGURE 1: Block diagrams of the angle calculation methods using Kalman filter tested in this paper.

magnitude of influence of impact and motion accelerations. That is, it was assumed that the angle difference involves substantial error of angle calculated from acceleration signals, which is caused by impact and movement accelerations. The value of noise ratio is varied as follows:

$$\begin{aligned} n &= n_1, \quad \text{for } \left|\hat{\theta} - \theta_{acc}\right| \le \theta_1, \\ n &= n_2, \quad \text{for } \theta_1 < \left|\hat{\theta} - \theta_{acc}\right| \le \theta_2, \\ n &= n_3, \quad \text{for } \theta_2 < \left|\hat{\theta} - \theta_{acc}\right| \le \theta_3, \\ n &= n_4, \quad \text{for } \theta_3 < \left|\hat{\theta} - \theta_{acc}\right|, \end{aligned} \tag{6}$$

where, n and $|\hat{\theta} - \theta_{acc}|$ represent the noise ratio and the angle difference between the angle estimated by the Kalman filter $\hat{\theta}$ and the angle calculated from acceleration signals θ_{acc}, respectively. The angle difference $|\hat{\theta} - \theta_{acc}|$ shows approximately the magnitude of influence of impact and motion accelerations. θ_1, θ_2, and θ_3 show thresholds to change values of the noise ratio, respectively.

3. Methods of Validation Tests

The angle calculation methods were applied to data measured with inertial sensors and evaluated in comparison to those angles measured with an optical motion measurement system. First, the evaluation was performed in measurement of lower limb angles in treadmill walking with healthy subjects. Then, angles of a rigid body model were measured for evaluation of the methods, because some other studies evaluated their angle measurement method with inertial sensors using the rigid plate that fixed a sensor together with markers of an optical motion measurement system [4, 8, 10, 11].

3.1. Measurement of Lower Limb Angles in Treadmill Walking. Inclination angles of lower limb segments in treadmill walking were measured with 3 healthy subjects (male, 22-23 y.o.). The subjects walked on a treadmill for about 90 sec at speeds of 1 km/h (slow), 3 km/h (normal), and 5 km/h (fast). Five trials were performed for each walking speed.

Seven wireless inertial sensors (WAA-006, Wireless Technologies) were attached on the feet, the shanks and the thighs of both legs, and lumbar region with stretchable bands (Figure 2(a)). The sensors were put inside of pocket of the band. Acceleration and angular velocity signals of each sensor were measured with a sampling frequency of 100 Hz and were transmitted to a PC via Bluetooth network.

The optical motion measurement system (Optotrak, Northern Digital, Inc.) was used to measure reference data for evaluating angles calculated by the methods from data measured with the inertial sensors. Markers for reference data were attached on the left side of the body (Figure 2(a)). The maker positions were measured with a sampling frequency of 100 Hz.

3.2. Measurement of Angles with a Rigid Body Model. Figure 2(b) shows the schematic diagram of the rigid body model used in the measurement. The rigid body model simulated motion of the thigh, the shank, and the knee joint. The optical motion measurement system (Optotrak, Northern Digital, Inc.) was also used to measure reference data for evaluating the angle calculation method. Sensors and markers were attached on the rigid body model as shown in Figure 2(b). Acceleration and angular velocity signals of each sensor and the marker positions were measured with sampling frequency of 100 Hz.

Inclination angles of the thigh and the shank parts were measured for 35 sec with angle ranges of ±15, ±30, ±45, ±60, and ±75 deg for the thigh part. Zero degree means the direction of gravitational force. The shank part was moved freely associated with movement of the thigh part. The cycle period of the movements was 2 sec, and five trials were conducted for each target angle range.

4. Results of Validation Tests

Two variable-Kalman-gain methods were evaluated in comparison to the previous fixed-Kalman-gain method. Here, for

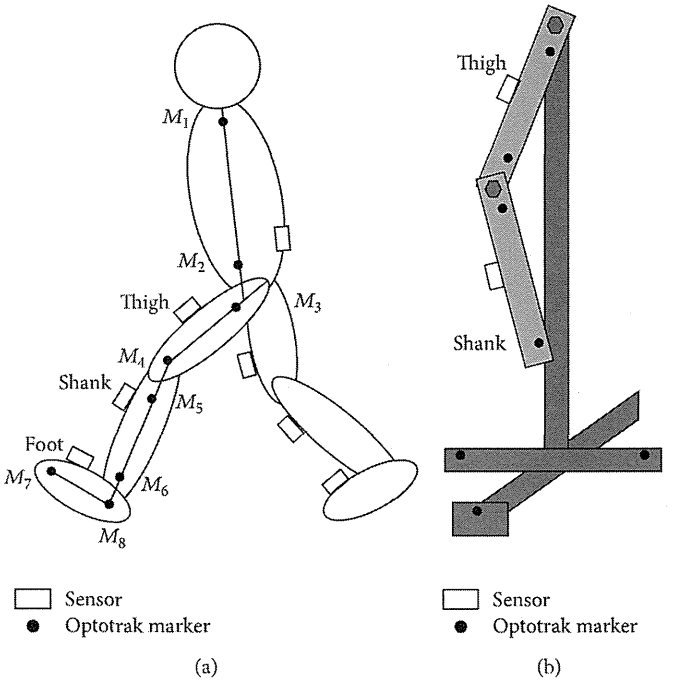

FIGURE 2: Experimental setup for the angle measurement during treadmill walking (a) and the angle measurement using rigid body model (b). M1: the acromion, M2: along the long axis of the trunk at the same height as the iliospinale anterius, M3: the great trochanter, M4: the lateral femoral condyle, M5: the caput fibulae, M6: the lateral malleolus, M7: the metatarsale fibulare, and M8: on the foot at the same height as the metatarsale fibulare along the line of shank markers.

the fixed-gain method, values of the noise ratio n to determine Kalman gain and the cutoff frequency of Butterworth low-pass filter for acceleration signals f_c are shown below.

Method 1 (previous fixed Kalman gain method)

$$n = 10^6, \qquad f_c = 0.5\,\text{Hz}. \tag{7}$$

Method 2 (fixed Kalman gain method)

$$n = 10^6, \qquad f_c = 10\,\text{Hz}. \tag{8}$$

Method 1 is the previous method used in our research group, in which the noise ratio of Kalman filter was fixed and cutoff frequency of the low-pass filter for acceleration signals was determined to remove impact and motion accelerations. Method 2 is the fixed-Kalman-gain method with higher cutoff frequency of the low-pass filter, which was tested to make clear the influence of low cutoff frequency on measurement error.

There was offset difference between the sensor system and camera-based motion analysis system, because the markers for the reference signals were not attached on the sensors. Therefore, the difference was calculated as the mean value of the first 100 samples of the 1st measurement and removed the value for evaluation. Then, root mean squared error (RMSE) and correlation coefficient (ρ) between measured angles with sensors and reference values were calculated for evaluating measurement accuracy. In this paper, inclination angles of lower limb segments in the sagittal plane were evaluated.

4.1. Measurement of Lower Limb Angles in Treadmill Walking. For the variable-Kalman-gain methods, values of the noise ratio n and threshold values were determined by trial and error as shown below.

Method 3 (variable-gain method based on acceleration magnitude)

$$\begin{aligned} n &= 10^4, \quad \text{for } |\alpha| \le 20\,\text{mG}, \\ n &= 10^6, \quad \text{for } 20\,\text{mG} < |\alpha| \le 300\,\text{mG}, \\ n &= 10^8, \quad \text{for } 300\,\text{mG} < |\alpha| \le 1\,\text{G}, \\ n &= 10^{13}, \quad \text{for } 1\,\text{G} < |\alpha|. \end{aligned} \tag{9}$$

Method 4 (variable-gain method based on angle error)

$$\begin{aligned} n &= 10^4, \quad \text{for } \left|\widehat{\theta} - \theta_{\text{acc}}\right| \le 1\ \text{deg}, \\ n &= 10^6, \quad \text{for } 1\ \text{deg} < \left|\widehat{\theta} - \theta_{\text{acc}}\right| \le 15\ \text{deg}, \\ n &= 10^8, \quad \text{for } 15\ \text{deg} < \left|\widehat{\theta} - \theta_{\text{acc}}\right| \le 60\ \text{deg}, \\ n &= 10^{13}, \quad \text{for } 60\ \text{deg} < \left|\widehat{\theta} - \theta_{\text{acc}}\right|. \end{aligned} \tag{10}$$

Here, the cutoff frequency of the low-pass filter for acceleration signals f_c was 10 Hz for both methods.

Figures 3 and 4 show RMSE values and ρ values of measured inclination angles, respectively. The proposed variable-gain method (Method 4) showed the smallest average RMSE

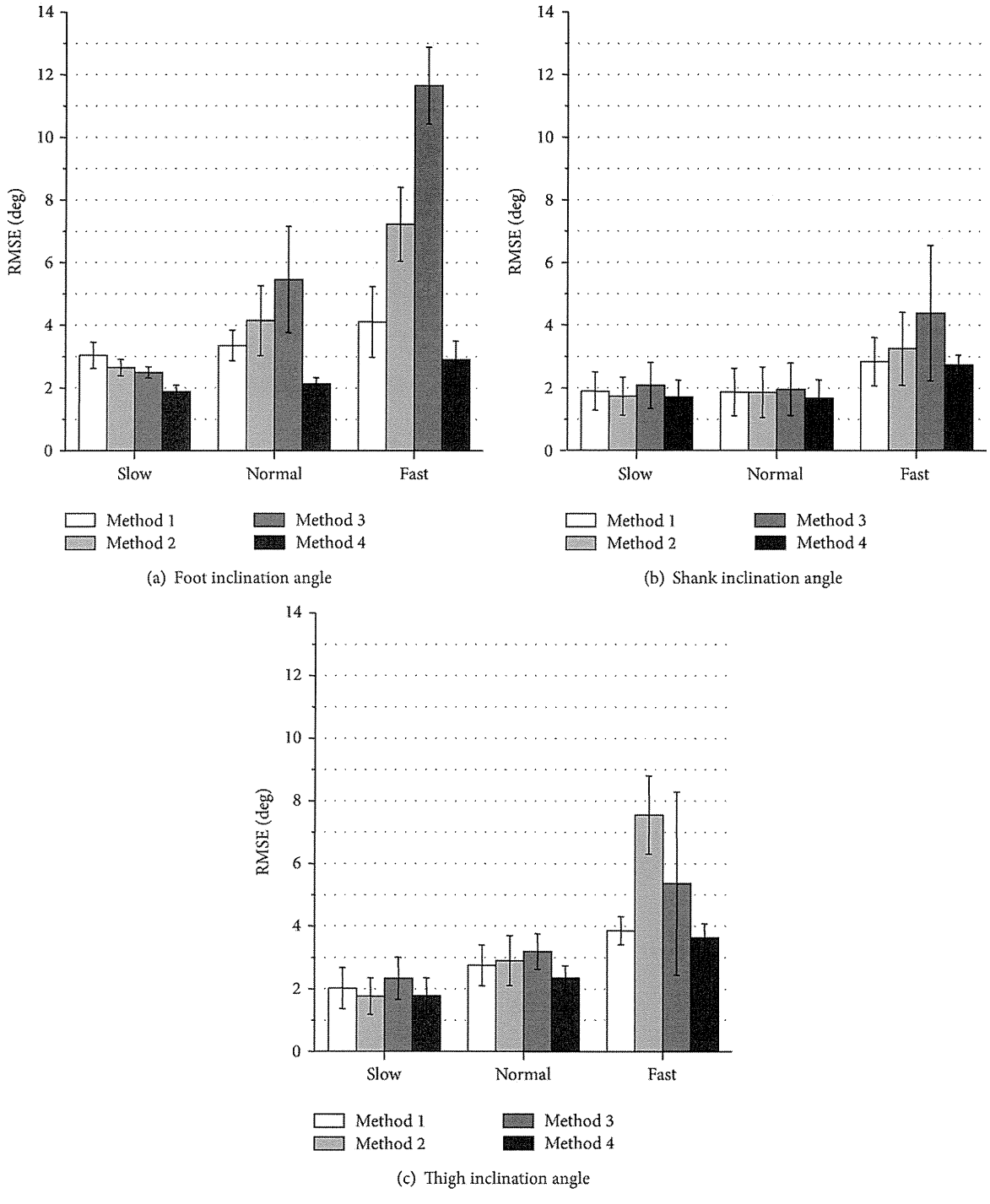

FIGURE 3: Evaluation results of RMSE of measured inclination angles during treadmill walking. Average values obtained from the results of 5 trials of all subjects are shown for each walking speed.

values and the largest ρ values for all of measurement conditions. Method 4 achieved average RMSE values of less than 3.0 deg except for thigh angle at fast walking speed and average values of correlation coefficient larger than 0.994 for all the measurement conditions.

The measurement accuracy of foot inclination angle was improved significantly with Method 4 for all walking speeds comparing to the results of Method 1 used in our previous studies (Figures 3(a) and 4(a)). For the shank and the thigh inclination angles, slight improvement of RMSE values and ρ values was shown for all walking speeds with Method 4 compared to the results of Method 1 (Figures 3(b), 3(c) and 4(b), 4(c)).

The values of RMSE with Method 2 (fixed-gain method with higher cut-off frequency) decreased compared to the results of Method 1 in all the segments at slow walking

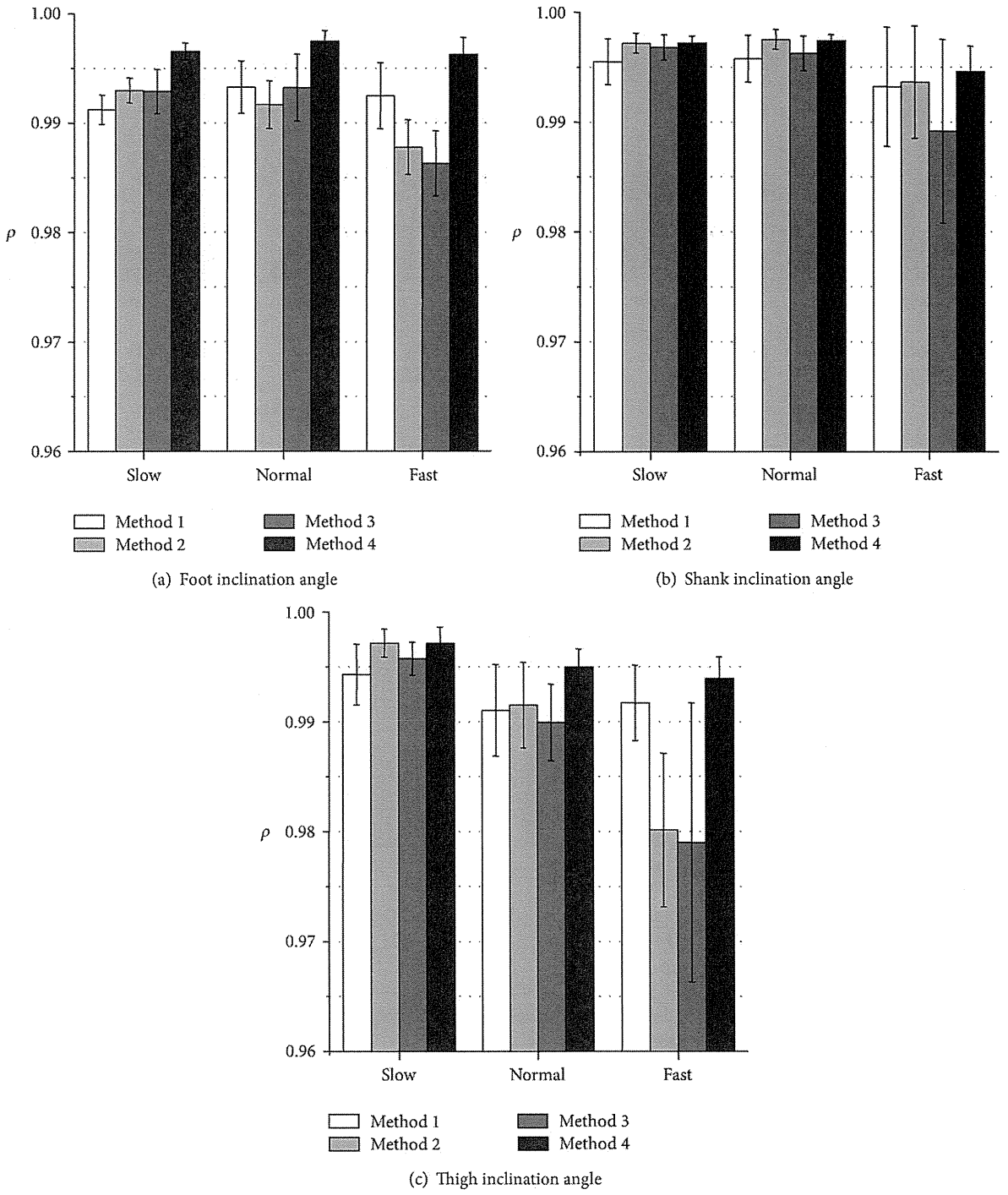

FIGURE 4: Evaluation results of correlation coefficient (ρ) of measured inclination angles during treadmill walking. Average values obtained from the results of 5 trials of all subjects are shown for each walking speed.

speed. However, at normal and fast walking speeds, the values of RMSE with Method 2 increased compared to the results of Method 1. Method 3 (variable-gain method based on acceleration magnitude) reduced measurement accuracy especially for fast waking speed and for foot inclination angle.

4.2. Measurement of Angles Using Rigid Body Model. The parameter values used for Methods 3 and 4 are shown below.

Method 3 (variable-gain method based on acceleration magnitude)

$$\begin{aligned} n &= 10^4, \quad \text{for } |\alpha| \leq 10\,\text{mG}, \\ n &= 3 \times 10^6, \quad \text{for } 10\,\text{mG} < |\alpha| \leq 200\,\text{mG}, \\ n &= 10^7, \quad \text{for } 200\,\text{mG} < |\alpha| \leq 400\,\text{mG}, \\ n &= 2 \times 10^7, \quad \text{for } 400\,\text{mG} < |\alpha|. \end{aligned} \tag{11}$$

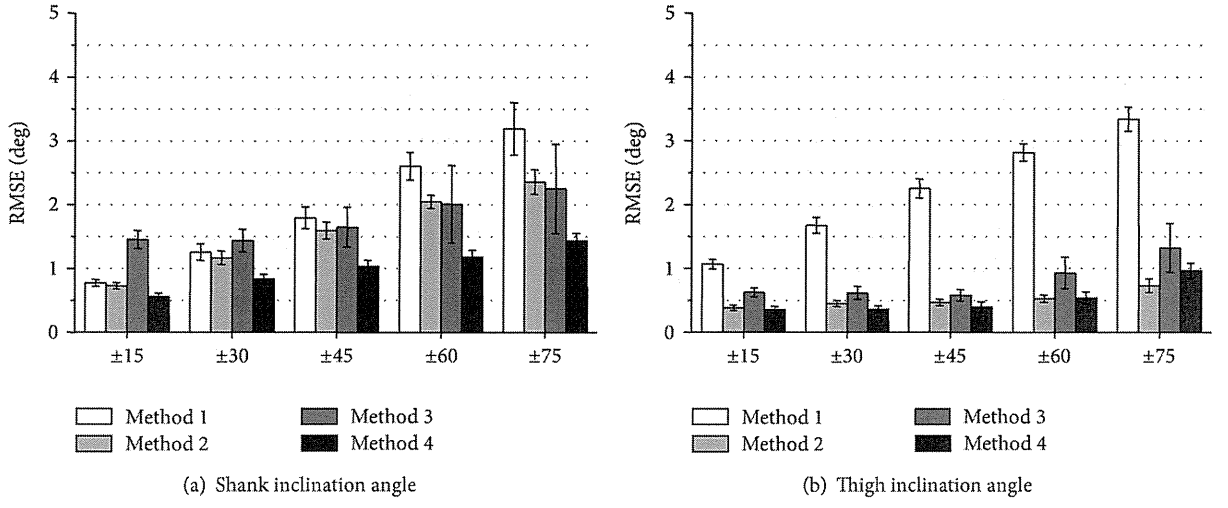

FIGURE 5: Evaluation results of RMSE of measured inclination angles using rigid body model. Average values obtained from the results of 5 trials are shown for each target angle range.

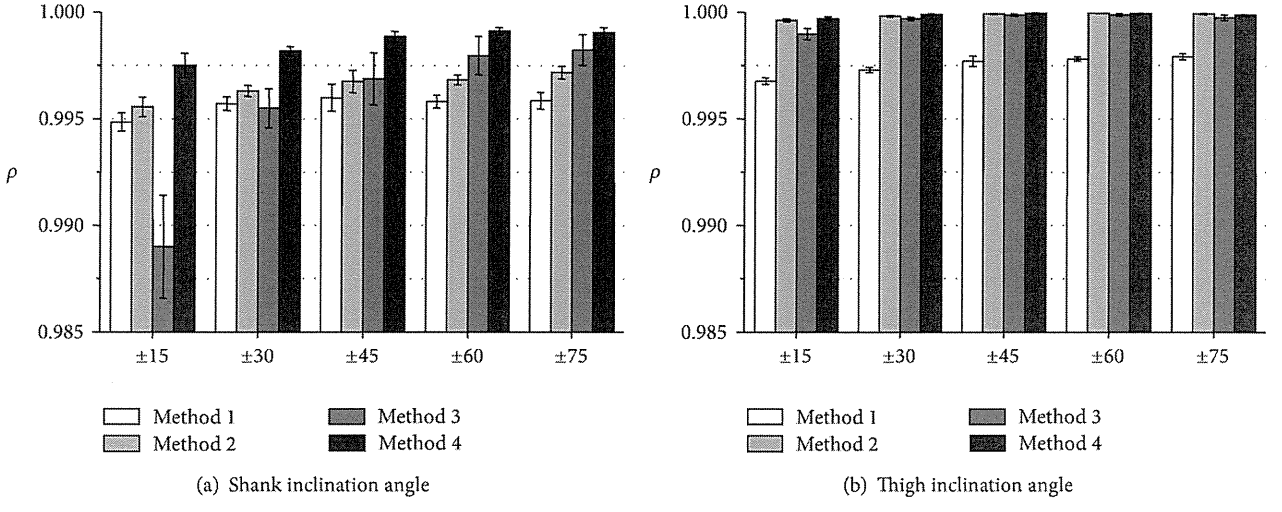

FIGURE 6: Evaluation results of correlation coefficient (ρ) of measured inclination angles using rigid body model. Average values obtained from the results of 5 trials are shown for each target angle range.

Method 4 (variable-gain method based on angle error)

$$\begin{aligned} n &= 10^4, \quad \text{for } \left|\hat{\theta} - \theta_{\text{acc}}\right| \le 1 \text{ deg}, \\ n &= 3 \times 10^6, \quad \text{for } 1 \text{ deg} < \left|\hat{\theta} - \theta_{\text{acc}}\right| \le 20 \text{ deg}, \\ n &= 10^7, \quad \text{for } 20 \text{ deg} < \left|\hat{\theta} - \theta_{\text{acc}}\right| \le 30 \text{ deg}, \\ n &= 2 \times 10^7, \quad \text{for } 30 \text{ deg} < \left|\hat{\theta} - \theta_{\text{acc}}\right|. \end{aligned} \tag{12}$$

Here, the cutoff frequency of the low-pass filter for acceleration signals f_c was 10 Hz for both methods. The parameter values of Methods 3 and 4 were changed from those values in angle measurement with human subjects, since magnitude of impact and motion acceleration signals and angle difference $|\hat{\theta} - \theta_{\text{acc}}|$ were smaller than that in the measurement with human subjects.

Figures 5 and 6 show RMSE values and ρ values of measured inclination angles, respectively. The proposed variable-gain method (Method 4) showed highest measurement accuracy almost for all the target angle ranges. Average values of RMSE and correlation coefficient with Method 4 were less than 1.5 deg and larger than 0.9975, respectively. Although Methods 2 and 3 were also effective to improve measurement accuracy, Method 3 could not improve shank angle in movements of target angle range of ±15 deg and ±30 deg.

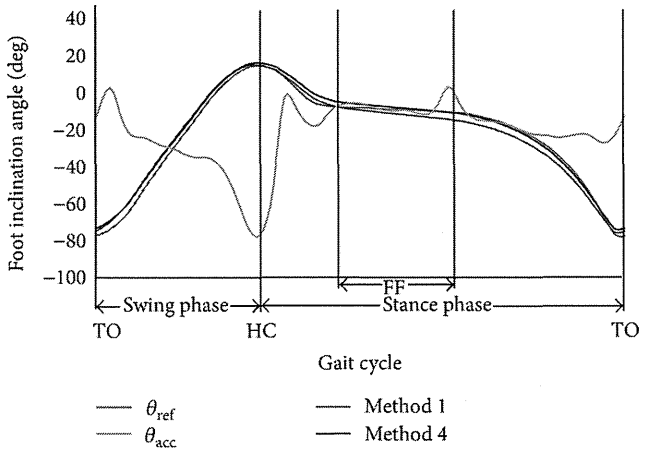

FIGURE 7: An example of waveforms of reference and measured foot inclination angles at normal walking speed. θ_{ref} and θ_{acc} represent reference angle and angle calculated from acceleration signals, respectively. The x-axis shows the gait cycle. The toe off, the heel contact, and the foot flat are represented by TO, HC, and FF, respectively.

5. Discussion

The proposed variable-Kalman-gain method (Method 4) measured lower limb angles in treadmill walking with the smallest average values of RMSE and the largest average values of correlation coefficient. In particular, Method 4 showed significant improvement in calculation of foot inclination angle in treadmill walking compared to our previous method (Method 1). It is a useful result that measurement accuracy of foot inclination angle was improved, because evaluation of foot movements in walking is important for gait of motor disabled subjects and elderly persons. In measurement of shank and thigh angles, values of the noise ratio were not so greatly varied, since magnitude of the angle difference $|\hat{\theta} - \theta_{acc}|$ did not fluctuate significantly during movements. This is one of the reasons why improvement of measurement accuracy was not so large in shank and thigh angles with Method 4.

The proposed variable-Kalman-gain method (Method 4) was highly effective in calculation of foot inclination angle. Figure 7 shows the reference and calculated foot inclination angles of one gait cycle at normal walking speed. As seen in Figure 7, the calculated angle with Method 4 was almost equal to that with Method 1 between around the TO and the HC in the swing phase. Method 4 improved angle calculation between around the FF and the TO in the stance phase. It is considered that the sensor attached on the foot was close to the stationary state at around the FF. At that time, the variable-Kalman-gain method corrected the angle significantly increasing values of Kalman gain (decreasing noise ratio), since the angle difference $|\hat{\theta} - \theta_{acc}|$ was small as the influence of impact and movement accelerations was small. It is possible to decrease angle measurement error between the FF and the TO by reducing noise ratio with Method 1. However, in that case, angle error between around the TO and the HC is increased by the influence of impact and movement accelerations. Method 4 reduced Kalman gain effectively at around the TO and the HC, since the angle difference $|\hat{\theta} - \theta_{acc}|$ increased. Therefore, the Method 4 could be effective especially in foot angle measurement, decreasing the influence of impact and motion accelerations.

As shown in Figure 3, RMSE values of measured inclination angles in treadmill walking with Method 2 decreased at slow walking speed compared to the results of Method 1 in all segments. In addition, as shown in Figure 5, RMSE values of measured inclination angles of the rigid body model with Method 2 decreased at all target angle ranges compared to the results of Method 1 for both segments. These suggest that very low cutoff frequency for the low-pass filtering of the acceleration signal increases measurement error if impact and movement accelerations are not so large. The cause of error increases in treadmill walking at the normal and fast walking speeds with Method 2 is considered to be influences of impact and motion accelerations. It is considered that although 0.5 Hz of cutoff frequency is reasonable value for removing impact and motion accelerations in angle calculation of human gait, error increase is caused by the large delay in the low pass filtering.

The variable-gain method based on acceleration magnitude (Method 3) did not show improvement of measurement accuracy of lower limb angles of human gait. For most of measurement conditions, average values of RMSE increased, and those of correlation coefficient decreased. The parameter values that are good for changing Kalman gain used in (9)–(12) were determined by trial and error method for both variable-gain methods. Although there is a possibility of improving measurement accuracy with Methods 3 and 4, the results of this paper suggest that the proposed method of changing the Kalman gain based on angle error was more suitable to the Kalman filter used in our system than that based on acceleration magnitude.

In angle measurement of the rigid body model, the values of RMSE with Method 4 were less than 1.5 deg for all segments and all target angle ranges. Those RMSE values

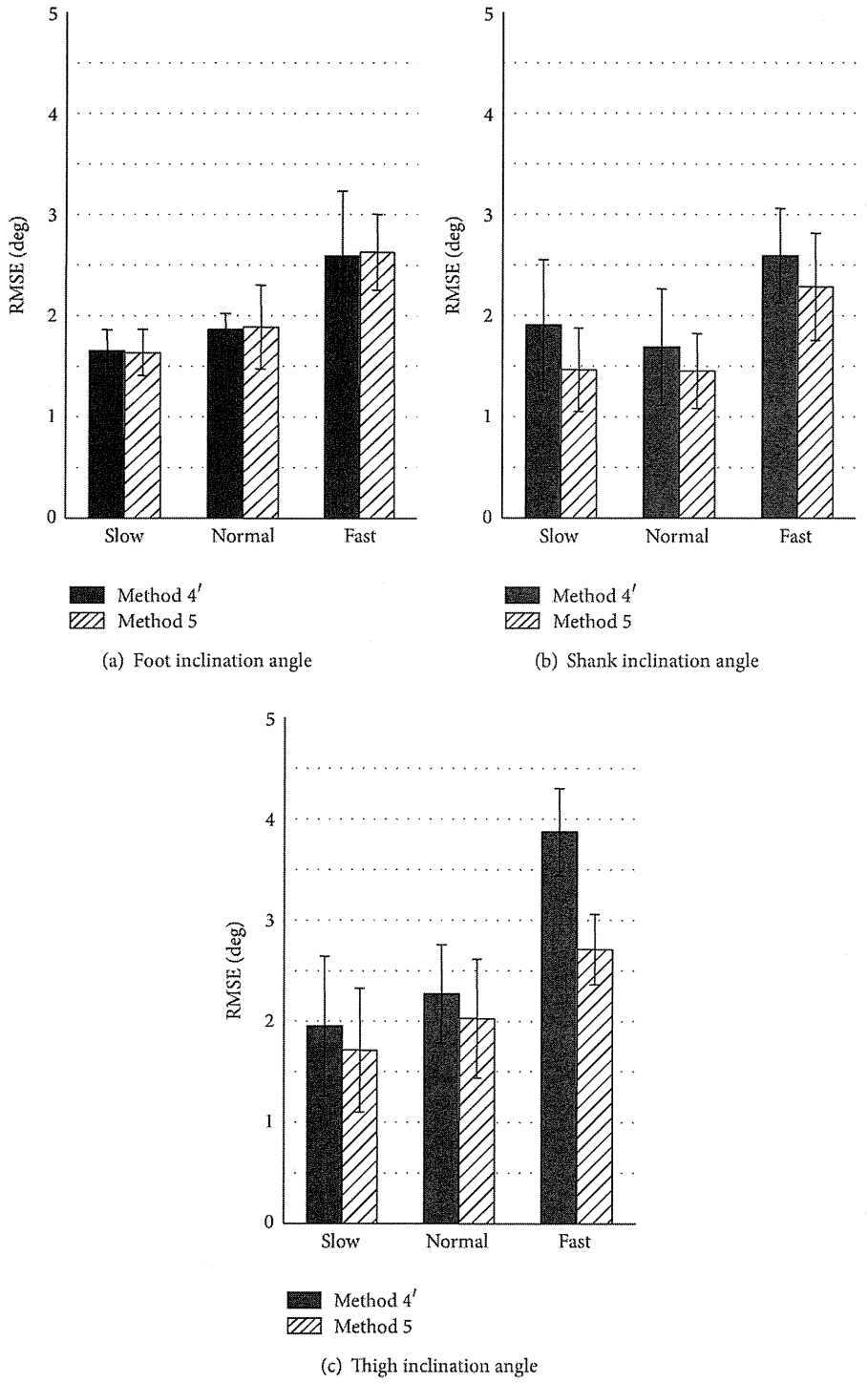

FIGURE 8: Average values of RMSE of measured inclination angles during treadmill walking calculated by using Methods 4 and 5.

show measurement accuracy similar to or higher than results seen in other studies that used markers of camera-based motion measurement system fixing on a rigid plate together with the sensor or on the sensor directly [4, 8, 10, 11]. It is considered that the proposed variable-gain method became effective in measurement of human gait.

In the proposed variable-gain method, influence of impact and motion accelerations was approximately represented by $|\hat{\theta} - \theta_{acc}|$. Here, the approximation was validated by comparing to results of using $|\theta_{ref} - \theta_{acc}|$ as shown in Figure 8, in which θ_{ref} shows reference value measured with the camera-based motion measurement system. In the

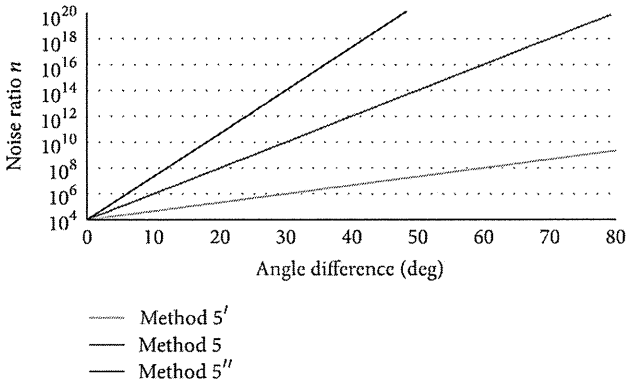

FIGURE 9: Relationships between the noise ratio and the angle difference used in the test of influence of the noise ratio.

comparison, the noise ratio (Kalman gain) was determined as continuous value by the followings from the angle difference.

Method 4′:

$$n = 10^4 e^{0.46\cdot|\widehat{\theta}-\theta_{acc}|}. \tag{13}$$

Method 5:

$$n = 10^4 e^{0.46\cdot|\theta_{ref}-\theta_{acc}|}. \tag{14}$$

Here, (13) and (14) were derived by linear approximation of discrete values of the noise ratio n in (10). That is,

$$\log n = ax + \log b, \tag{15}$$

where a and b represent constant values and x represents the angle difference. The constant value a was determined to decrease RMSE values by trial and error method, and b was set 10^4 from (10). As shown in Figure 8, for foot inclination angles, measurement results with Method 5 were similar to the results with Method 4′ for all walking speeds. Measurement results for the shank and the thigh inclination angles were improved for all walking speeds with Method 5 using reference values. Average values of RMSE with Method 5 were less than 3.0 deg for all walking speeds and all segments. This result suggests that the proposed variable-Kalman-gain method based on angle error is effective to improve measurement accuracy of angle during human gait. It is also suggested that measurement accuracy with Method 4′ can be improved if error in $|\widehat{\theta} - \theta_{acc}|$ is reduced.

Angle measurement accuracy depends on the noise ratio. In this paper, parameter values to calculate values of noise ratio used in (9)–(14) were determined to decrease RMSE values by trial and error method. Here, different relationships between the noise ratio and the angle difference described by (14) were examined. Figures 9 and 10 show the tested relationships and results of their measurement accuracy, respectively. Method 5′ used smaller noise ratio and Method 5″ used larger noise ratio than Method 5. In Figure 10, the results obtained by Method 1 (fixed-gain method) are also shown. The RMSE values were decreased with variable-gain method in any parameter setting compared to the fixed-gain method. However, Method 5′ (smaller noise ratio) showed larger RMSE values than Method 5 for all the measurement conditions. It is considered that the influence of impact and movement accelerations was not decreased sufficiently with Method 5′ because of large value of Kalman gain (small noise ratio). On the other hand, RMSE values with Method 5″ (larger noise ratio) were similar to that of Method 5 for almost all the measurement conditions. However, Method 5″ has a tendency to increase RMSE values of the thigh and the shank inclination angles for the fast walking speed. Therefore, further studies on the method to determine appropriate Kalman gain are expected. In addition, this paper focused only on the error of angle calculated from acceleration signals in determination of Kalman gain. It is considered that the noise ratio also depends on magnitude of the offset drift of gyroscope. This is also required to be studied more for measurement of angles with the variable-gain Kalman filter. Finally, the proposed variable-Kalman-gain method was validated in measurement of inclination angles of lower limb segments in the sagittal plane in this paper. It is expected to show the effectiveness of the proposed method in measurement of 3 dimensional angles.

6. Conclusion

In this paper, variable-gain Kalman filter was tested to improve measurement accuracy of lower limb angles during gait, in which two calculation methods of Kalman gain were compared to fixed-gain Kalman filter. In measurements of lower limb angles of healthy subjects in treadmill walking and that of angles of a rigid body model, the variable-gain method based on the angle difference proposed in this study showed the highest measurement accuracy for most of measurement conditions. In particular, the proposed variable-gain method improved significantly measurement accuracy of foot inclination angle in human gait. On the other hand, measurement results of the shank and the thigh inclination angles show slight improvement of measurement accuracy. The proposed variable-gain method was found to be effective in angle measurement with inertial sensors. The

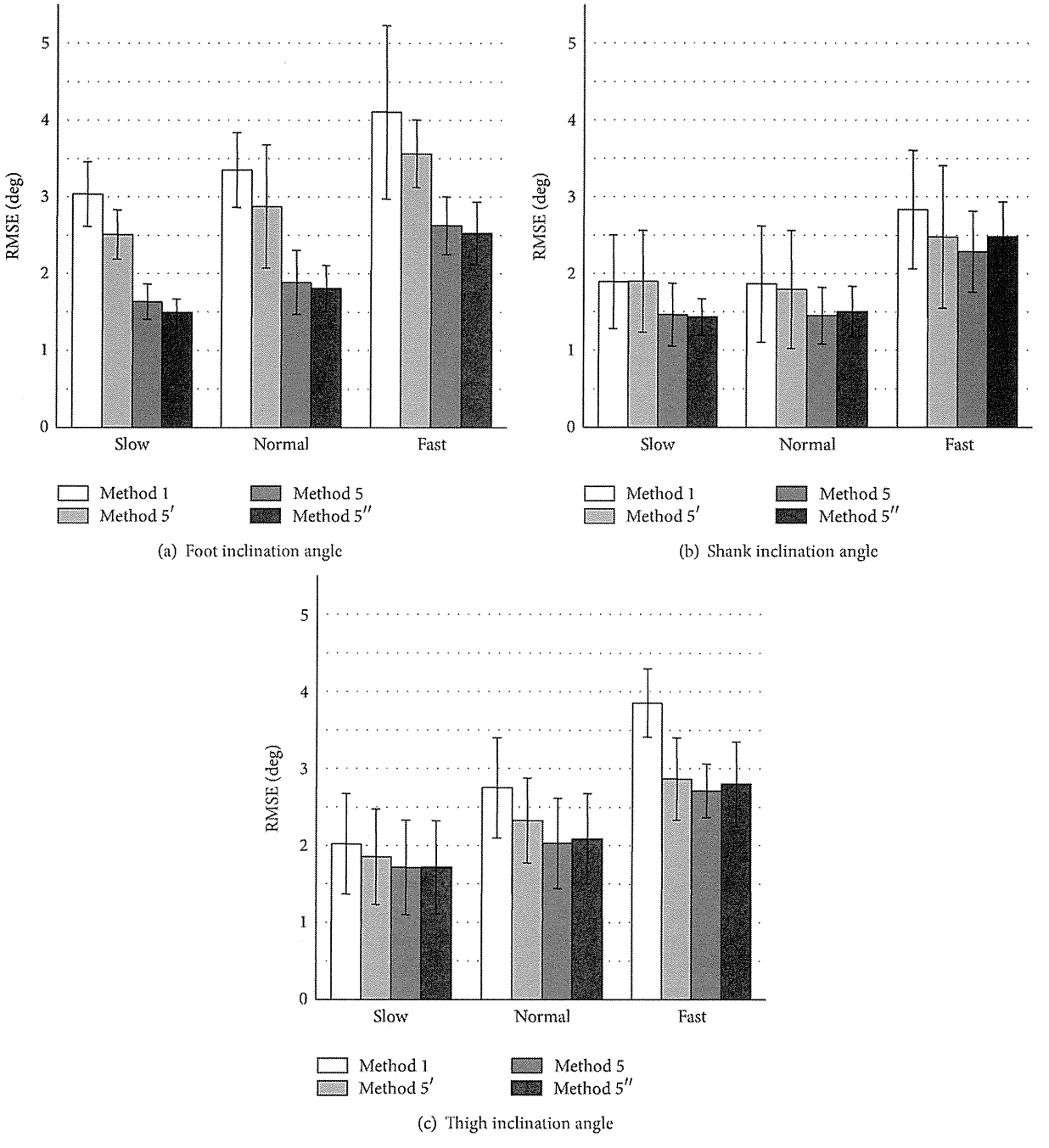

FIGURE 10: Average RMSE values of measured inclination angles during treadmill walking calculated by fixed-gain method (Method 1) and variable-gain method with 3 different parameter settings for the noise ratio.

results also suggested that more accurate measurement can be realized by improving estimation accuracy of the angle difference $|\theta_{ref} - \theta_{acc}|$. Further studies on this point and to find appropriate method to determine Kalman gain using the angle difference and other parameters are expected.

Acknowledgment

This work was supported in part by the Ministry of Education, Culture, Sports, Science and Technology of Japan under a Grant-in-Aid for Challenging Exploratory Research.

References

[1] K. Tong and M. H. Granat, "A practical gait analysis system using gyroscopes," *Medical Engineering and Physics*, vol. 21, no. 2, pp. 87–94, 1999.

[2] H. Dejnabadi, B. M. Jolles, and K. Aminian, "A new approach to accurate measurement of uniaxial joint angles based on a combination of accelerometers and gyroscopes," *IEEE Transactions on Biomedical Engineering*, vol. 52, no. 8, pp. 1478–1484, 2005.

[3] J. C. Alvarez, R. C. González, D. Alvarez, A. M. López, and J. Rodríguez-Uría, "Multisensor approach to walking distance estimation with foot inertial sensing," in *Proceedings of the 29th*

Annual International Conference of IEEE-EMBS, Engineering in Medicine and Biology Society (EMBC '07), pp. 5719–5722, August 2007.

[4] D. Roetenberg, P. J. Slycke, and P. H. Veltink, "Ambulatory position and orientation tracking fusing magnetic and inertial sensing," *Transactions on Biomedical Engineering*, vol. 54, no. 5, pp. 883–890, 2007.

[5] S. J. M. Bamberg, A. Y. Benbasat, D. M. Scarborough, D. E. Krebs, and J. A. Paradiso, "Gait analysis using a shoe-integrated wireless sensor system," *IEEE Transactions on Information Technology in Biomedicine*, vol. 12, no. 4, pp. 413–423, 2008.

[6] A. Findlow, J. Y. Goulermas, C. Nester, D. Howard, and L. P. J. Kenney, "Predicting lower limb joint kinematics using wearable motion sensors," *Gait and Posture*, vol. 28, no. 1, pp. 120–126, 2008.

[7] R. Takeda, S. Tadano, A. Natorigawa, M. Todoh, and S. Yoshinari, "Gait posture estimation using wearable acceleration and gyro sensors," *Journal of Biomechanics*, vol. 42, no. 15, pp. 2486–2494, 2009.

[8] M. D. Djurić-Jovičić, N. S. Jovicic, D. B. Popović, and A. R. Djordjević, "Nonlinear optimization for drift removal in estimation of gait kinematics based on accelerometers," *Journal of Biomechanics*, vol. 45, no. 16, pp. 2849–2854, 2012.

[9] C. Mazzà, M. Donati, J. McCamley, P. Picerno, and A. Cappozzo, "An optimized Kalman filter for the estimate of trunk orientation from inertial sensors data during treadmill walking," *Gait and Posture*, vol. 35, no. 1, pp. 138–142, 2012.

[10] B. J. E. Misgeld, D. Ruschen, S. Kim, and S. Leonhardt, "Body sensor network-based strapdown orientation estimation: application to human locomotion," in *International Conference on Rehabilitation Robotics (ICORR '13)*, 2013.

[11] A. Caroselli, F. Bagala, and A. Cappello, "Quasi-real time estimation of angular kinematics using single-axis accelerometers," *Sensors*, vol. 13, no. 1, pp. 918–937, 2013.

[12] J. M. Jasiewicz, J. H. J. Allum, J. W. Middleton et al., "Gait event detection using linear accelerometers or angular velocity transducers in able-bodied and spinal-cord injured individuals," *Gait and Posture*, vol. 24, no. 4, pp. 502–509, 2006.

[13] H. Lau and K. Tong, "The reliability of using accelerometer and gyroscope for gait event identification on persons with dropped foot," *Gait and Posture*, vol. 27, no. 2, pp. 248–257, 2008.

[14] H. Saito and T. Watanabe, "Kalman-filtering-based joint angle measurement with wireless wearable sensor system for simplified gait analysis," *IEICE Transactions on Information and Systems*, vol. 94, no. 8, pp. 1716–1720, 2011.

[15] T. Watanabe and H. Saito, "Tests of wireless wearable sensor system in joint angle measurement of lower limbs," in *Proceedings of the 33rd Annual International Conference of the IEEE Engineering in Medicine and Biology Society (EMBS '11)*, pp. 5469–5472, September 2011.

[16] A. M. Sabatini, "Quaternion-based extended Kalman filter for determining orientation by inertial and magnetic sensing," *IEEE Transactions on Biomedical Engineering*, vol. 53, no. 7, pp. 1346–1356, 2006.

Reorientation of a Nonspherical Capsule in Creeping Shear Flow

Toshihiro Omori,[1,*] Yohsuke Imai,[2] Takami Yamaguchi,[1] and Takuji Ishikawa[2,†]

[1]*Department of Biomedical Engineering, Tohoku University, Aoba 6-6-01 Sendai Miyagi, Japan*
[2]*Department of Bioengineering and Robotics, Tohoku University, Aoba 6-6-01 Sendai Miyagi, Japan*
(Received 24 August 2011; published 28 March 2012)

The dynamics of a capsule and a biological cell is of great interest in chemical engineering and bioengineering. Although the dynamics of a rigid spheroid is well understood by Jeffery's theory, that of a spheroidal capsule remains unclear. In this Letter, the motion of a spheroidal capsule or a red blood cell in creeping shear flow is investigated. The results show that the orientation of a nonspherical capsule is variant under time reversal, though that of a rigid spheroid is invariant. Surprisingly, the alignment of a nonspherical capsule over a long time duration shows a transition depending on the shear rate, which can be utilized for a particle-alignment technique. These findings form a fundamental basis of the suspension mechanics of capsules and biological cells.

DOI: 10.1103/PhysRevLett.108.138102 PACS numbers: 47.63.mf, 83.50.−v, 87.16.D−

About a century ago, Jeffery analytically derived the motion of a nonspherical object in creeping linear background flow [1]. Since then, Jeffery's theory has been used to describe the alignment of rods and ellipsoids, such as bacteria, platelets, etc. The theory states that the trajectory of a non-Brownian rigid ellipsoid in Stokes flow is invariant under time reversal and that reorientation over a long time duration does not occur under simple shear flow conditions. The time reversibility can be destroyed by introducing inertia effects [2] or viscoelastic properties of the surrounding fluid [3], because the motion is no longer independent of time in these cases. However, the effect of particle deformability on the time reversibility is not well clarified. This study investigates this question by using a capsule as a model deformable object.

A capsule is a liquid drop enclosed by a deformable membrane, which is of great interest in the chemical engineering, bioengineering, and food industries. Many capsules in realistic situations are not perfect spheres because of the inhomogeneity of the membrane properties or folding due to unbalanced osmotic pressure. If one places a nonspherical capsule in creeping shear flow, how does the orientation change relative to the flow field over a long time duration? Jeffery speculated that an ellipsoid may alter its orientation so that the viscous energy dissipation of the system becomes minimal [1]. However, this may not be true for a capsule with a large deformation. Although many former studies have examined the dynamics of a nonspherical capsule [4–8], none of them can answer this question.

In this Letter, the motion of a non-Brownian spheroidal capsule or a red blood cell (RBC) in creeping shear flow is investigated numerically. The results show that the orientation of a nonspherical capsule is variant under time reversal, although the orientation of a rigid ellipsoid is invariant. Surprisingly, the alignment of a nonspherical capsule over a long time duration shows a transition depending on the shear rate. The transition cannot be explained by the minimum energy dissipation, as speculated by Jeffery; the full fluid and solid mechanics are necessary to understand this phenomenon. The obtained results can be utilized for particle-alignment techniques in engineering applications and shed light on the complex dynamics of capsules and biological cells.

A capsule is assumed to be filled with an incompressible Newtonian fluid of viscosity $\lambda\mu$ and freely suspended in another fluid with the same density but viscosity μ. When the thickness of the capsule wall is small compared to its size and radius of curvature, the membrane can be modeled as a 2D hyperelastic surface without bending rigidity. In this study, we use two kinds of constitutive laws for the membrane: the neo-Hookean (NH) law [9] and the Skalak (SK) law [10]. The NH law describes isotropic volume-incompressible rubberlike material properties, whereas the Skalak law expresses the area incompressibility of a biological membrane.

To calculate capsule deformation accurately, fluid-structure interactions between the motion of the internal and external fluids and that of the capsule membrane have to be solved precisely. We assume that the flow is Stokesian, i.e., inertia-free, and the flow field is solved by a boundary element method. A finite element method is employed to solve the membrane mechanics. The governing equations and numerical methods are the same as in Refs. [6,11], and the details are explained in Ref. [12]. The reference shape of the capsule is assumed to be spheroid or biconcave, in the same manner as in Refs. [5,6]. The aspect ratio between the principal axes of the spheroid is represented by α. A linear triangular mesh with 5120 elements is used to discretize the membrane. The validation of the numerical methods is presented in Ref. [12].

In a Cartesian reference frame with the capsule center as the origin, the undisturbed linear background flow $\mathbf{v}^\infty$ can be described as $\mathbf{v}^\infty = (\mathbf{E} + \mathbf{\Omega}) \cdot \mathbf{x}$, where $\mathbf{E}$ and $\mathbf{\Omega}$ are the

 © 2012 American Physical Society

rate of strain and rotation tensors, respectively. In this study, we use two types of background flow: (a) a simple shear flow given by $E_{xy} = E_{yx} = \Omega_{xy} = -\Omega_{yx} = \frac{\dot{\gamma}}{2}$ (all the other components $= 0$), as shown in Fig. 1(a), and (b) an oscillatory planar elongational flow given by $E_{xy} = E_{yx} = \frac{\dot{\gamma}}{2}\cos\omega t$ (all the other components $= 0$), as shown in Fig. 1(b). Here, $\dot{\gamma}$ is the shear rate or the elongational rate, t is the time, and ω is the angular velocity of the flow, which is correlated to the oscillation period T as $T = 2\pi/\omega$. The capillary number Ca represents the ratio of the viscous force to the elastic force and is given by $\mathrm{Ca} = \mu\ell\dot{\gamma}/G_s$, where G_s is the membrane shear modulus and ℓ is the radius of a sphere that has the same volume as the ellipsoid or the biconcave capsule.

We first investigate the motion of a spheroidal oblate capsule in simple shear flow and compare the results with those of a rigid spheroid. To examine the capsule orientation efficiently, we define the orientation vector **e** as a unit vector extending from the center of gravity and pointing to material point P located at the revolution axis of the unstressed spheroidal capsule. θ is defined as the angle between **e** and the z axis, as shown in Fig. 1(c). At time $t = 0$, the oblate capsule without prestress is placed at an initial angle θ_0 of $\pi/4$. The deformation at time $t > 0$ due to the background shear is calculated until the steady periodic motion is achieved.

The motions of an oblate capsule with Ca = 0.3 and 1.0 are shown in Fig. 2(a) and 2(b), respectively ($\alpha = 0.6$, $\lambda = 1$, and NH membrane). The time history of θ is also shown in Fig. 2(c) for 30 periods of rotation. The results of a rigid spheroidal with the same α [1] are also plotted in the figure for comparison. Because of the nonspherical reference shape of the capsule membrane, θ oscillates twice during one rotation. In addition to the short-time oscillation, θ tends to approach towards 0 or $\pi/2$, depending on Ca, over a long time duration. The reorientation of the capsules is also clear in observing Figs. 2(a) and 2(b), because the material point P, which is indicated as a blue dot in the figures, moves towards $z = 0$ when Ca = 0.3, whereas it moves towards the z axis when Ca = 1.0. We note that the final orientation is independent of the initial orientation; this was confirmed numerically by changing the initial orientation randomly. Such reorientation did not happen for a rigid spheroid, as shown in Fig. 2(c). These results clearly illustrate that a deformable capsule becomes reoriented, even in simple shear flow, and the time reversibility of Jeffery's orbit can be destroyed by introducing particle deformability.

The results of Fig. 2 raise another important question about why the reorientation direction shows a transition with increasing Ca. We calculated the viscous energy dissipation due to the capsule motion to determine whether the transition occurred to minimize the dissipation energy. However, we did not observe a one-to-one correlation between the capsule reorientation and the minimum energy dissipation. Thus, the full fluid and solid mechanics must be examined to answer this question.

To understand the basic mechanism of the transition, we further simplify the background flow field by deleting the rotational contribution from the shear flow. When an oblate capsule with an arbitrary initial orientation is subjected to steady planar elongational flow, the orientation is finally directed towards the compressing direction in all cases. Given that the reorientation transition does not appear in steady planar elongational flow, the unsteadiness in the flow field likely plays an important role in the transition.

Next, we apply oscillatory planar elongational flow, given by Fig. 1(b), to an oblate capsule. In this flow field, the elongational rate and changing frequency of the elongational direction can be independently controlled. At $t = 0$, the oblate capsule without prestress is placed at $\theta_0 = \pi/4$. The capsule motions for the second period of oscillation with $\omega/(\dot{\gamma}\pi) = 0.08$ and Ca = 0.3 and 1.0 are shown in Figs. 3(a) and 3(b) ($\alpha = 0.6$, $\lambda = 1$, and NH

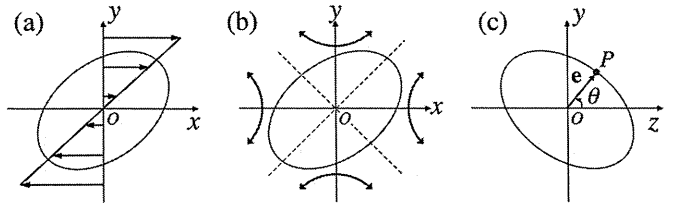

FIG. 1. Schematic illustration of a capsule in (a) simple shear flow and (b) oscillating planar elongational flow. (c) Orientation vector **e** is defined as a unit vector extending from the center of gravity and pointing to material point P. θ is defined as the angle between **e** and the z axis.

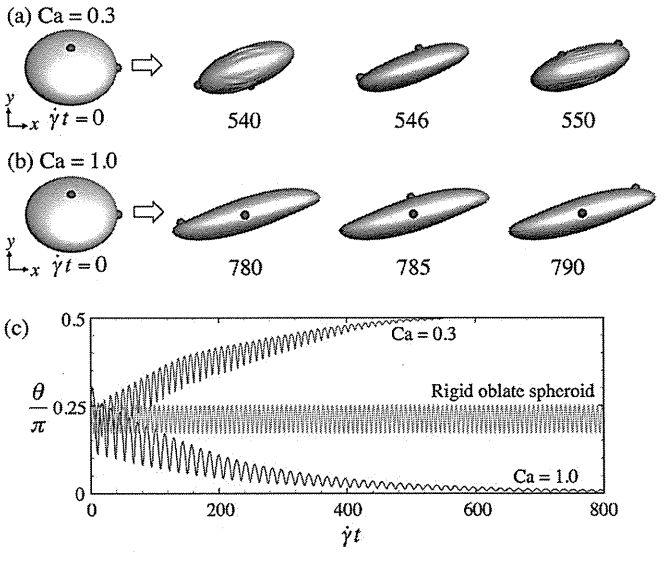

FIG. 2 (color). Oblate capsule in a simple shear flow with (a) Ca = 0.3 and (b) 1.0 ($\alpha = 0.6$, $\lambda = 1$, and NH membrane). Blue and red dots are material points on the membrane and are plotted as tracers. (c) Time change of θ, where the result of a rigid spheroid with same α [1] is also plotted for comparison.

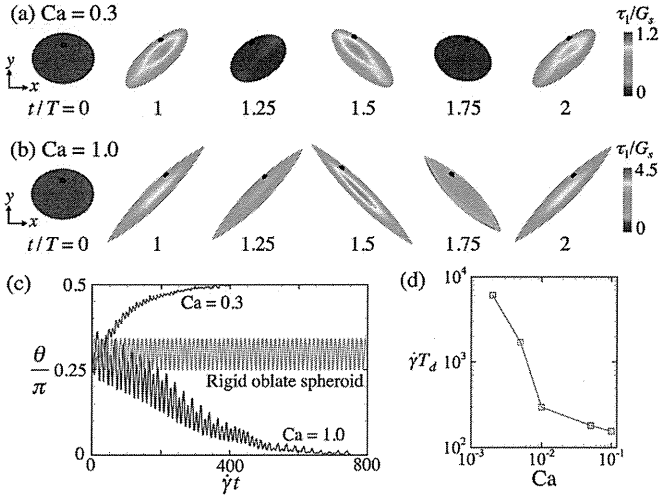

FIG. 3 (color). Motion of an oblate capsule in oscillating planar elongational flow with $\omega/(\dot{\gamma}\pi) = 0.08$ and (a) Ca = 0.3 or (b) Ca = 1.0 ($\alpha = 0.6$, $\lambda = 1$, and NH membrane). A black dot is placed at P as a tracer. (c) Time change of θ, where the result of a rigid spheroid with the same α [1] is plotted for comparison. (d) Dimensionless drift time in the small Ca regime.

membrane). Color contours show the distribution of τ_1, where τ_i is the in-plain principal elastic tension and $\tau_1 \geq \tau_2$. The time history of θ is also shown in Fig. 3(c) for 30 periods of oscillation. When Ca = 0.3, θ approaches to $\pi/2$ after a sufficient time duration, whereas when Ca = 1.0, θ approaches to 0. For Ca = 0.3, the capsule deformation is small at $t/T = 1.25$ and 1.75, when there is no background flow, and the τ_1 distributions at $t/T = 1.0$ and 1.5 are similar. For Ca = 1.0, however, large deformations remain at $t/T = 1.25$ and 1.75, resulting in a strong asymmetry in the τ_1 distribution between $t/T = 1.0$ and 1.5. Thus, the deformation is strongly affected by the time history in the high Ca regime, whereas it is quasisteady in the low Ca regime. This qualitative difference in the tension distribution likely causes the reorientation transition. When Ca is very small, the capsule should behave like a rigid body. In order to confirm the convergence, we calculate drift time T_d required for drifting from $\theta = \pi/4$ to $\pi/2$ and plot it in Fig. 3(d). We see that $\dot{\gamma}T_d$ increases rapidly as Ca is decreased, indicating convergence to the rigid body motion.

To clarify the reorientation phenomena in more detail, we plot a phase diagram of the final orientation as a function of Ca and $\omega/\dot{\gamma}\pi$. The oblate capsule is again subjected to the oscillatory planar elongational flow with $\theta_0 = \pi/4$. The computation is carried out for N periods of oscillation, and N is set to 30, as in Fig. 3(c). The convergence of the final angle is determined by the following equation: $|\theta_{30} - \theta_f| \leq \epsilon$, where θ_{30} is the average orientation vector of the 30th rotation, and $\theta_f = 0$, $\pi/2$, or θ_0. The threshold value of $\epsilon = 0.05$ is used in this study, because the results with $\epsilon = 0.1$ and 0.05 are almost the same. When the convergence criteria is not satisfied, we determined that the reorientation is in the transit regime.

The results of the phase diagram are shown in Fig. 4. The red region ($\theta_{30} \approx \theta_0$) indicates the rigid body motion or high frequency oscillation. When ω is very large, the capsule has little time to deform, which results in no obvious reorientation. When Ca $\rightarrow$ 0, the capsule motion converges to the rigid body motion. Figure 3(d) indicates that the red region also appears in the Ca < 0.001 regime when $\omega/\dot{\gamma}\pi = 0.08$, though the diagram in this small Ca region is not plotted due to extremely high computational load. The green region ($\theta_{30} \approx \pi/2$) indicates the quasisteady deformation. This region appears when ω is small, including the steady planar elongation ($\omega = 0$). The magenta region indicates infinite stretching. This region appears only when the membrane is strain-softening, such as NH membrane. A strain-hardening membrane can avoid this problem [13]. The black region ($\theta_{30} \approx 0$) indicates large unsteady deformation. This region appears only when the capsule is subjected to the large elongation with the moderate oscillating frequency. The phase diagram may be slightly affected by the selection of N. Since N is limited in terms of the computational cost, we cannot technically increase $N \rightarrow \infty$. These results clearly illustrate that the convergence of $\theta \rightarrow 0$ appears only when the large deformation is affected by the time history.

In the case of shear flow, the elongational direction relative to the material point on the membrane oscillates with the angular velocity of the membrane motion. Thus, one may assume ω as the average rotational velocity of a capsule in shear flow and draw the curve shown in Fig. 4. The results of an oblate capsule in shear flow, shown in Fig. 2, are plotted in Fig. 4 by circles. A curve with small

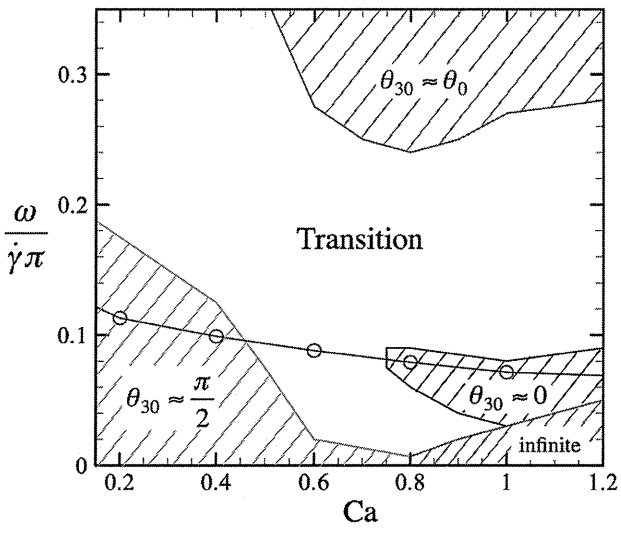

FIG. 4 (color). Phase diagram of the oblate capsule in oscillating elongational flow ($\alpha = 0.6$, $\lambda = 1$, and NH membrane). The circles in the figure indicate the converted results of the shear flow case.

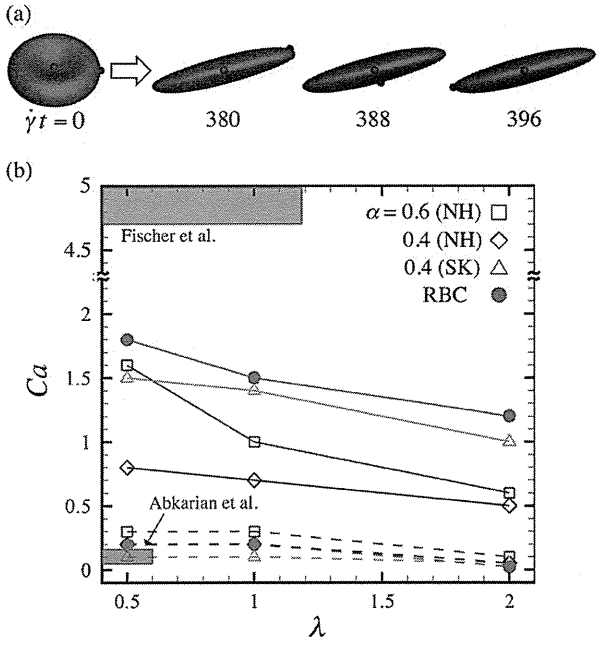

FIG. 5 (color). (a) Motion of a RBC in shear flow (Ca = 2.0, $\lambda = 1.0$). Blue and black dots are material points on the membrane and are plotted as tracers. (b) Effects of λ on the critical Ca number of oblate capsules and a RBC. The solid lines in the figure indicate Ca_0, and the broken lines indicate $\mathrm{Ca}_{\pi/2}$. Experimental conditions of Refs. [7,8] are plotted by gray and magenta regions, respectively.

Ca exists in the $\theta \to \pi/2$ region, whereas a curve with large Ca exists in the $\theta \to 0$ region. These results indicate that the reorientation transition found in the shear flow can also be explained by using Fig. 4.

Finally, we investigate the reorientation of a RBC in shear flow. The RBC membrane is modeled by the SK law with $C = 10$, where C is the ratio of area dilation to the shear modulus. Here we also investigate the effect of the viscosity ratio λ. Initially, the RBC is set to $\theta_0 = \pi/4$. The results of Ca = 2 and $\lambda = 1$ are shown in Fig. 5(a). Material point P, indicated as a blue dot in the figure, shifts to the z axis, i.e., $\theta \to 0$, for large Ca. When Ca was small, on the other hand, we confirmed that $\theta \to \pi/2$ in the same manner as the spheroidal capsule (data not shown). When $\theta = 0$, the RBC membrane has a pure tank-treading motion, and the membrane no longer oscillates during the rotation. When $\theta \neq 0$, on the other hand, the RBC shows a swinging motion, and the membrane oscillates during the rotation.

To effectively discuss the effect of λ and the constitutive law on the reorientation transition in shear flow, we define critical values of Ca: $\mathrm{Ca}_{\pi/2}$ indicates the maximum Ca value to show $\theta_{30} \approx \pi/2$ convergence, and Ca_0 indicates the minimum Ca value to show $\theta_{30} \approx 0$ convergence. The results of a RBC as well as spheroidal capsules with $\alpha = 0.4$ and 0.6 and with two types of membrane constitutive laws are shown in Fig. 5 as a function of λ. $\mathrm{Ca}_{\pi/2}$ and Ca_0 tend to decrease as λ increased. This is because the time history of deformation remains for a longer time as the inside viscosity increased, which leads to the transition in the smaller Ca conditions. The figure also indicates that the effect of the constitutive law is considerable. A capsule with the SK membrane tends to have a larger critical Ca_0 than that with the NH membrane. This is because the SK law shows the strain-hardening property, whereas NH law shows the strain-softening, so large deformations are suppressed by the SK membrane. Thus, the reorientation transition can be understood by considering the fluid and solid mechanics of capsule deformation.

In Fig. 5, experimental conditions of Refs. [7,8] are plotted by gray and magenta regions, respectively, by assuming $\mu = 11$–59 mPa · s, $\dot{\gamma} = 800\ \mathrm{s}^{-1}$ for Ref. [7] or 22–47 mPa · s and $\dot{\gamma} = 5\ \mathrm{s}^{-1}$ for Ref. [8], and $G_s = 4\ \mu\mathrm{N/m}$ and $\ell = 2.82\ \mu\mathrm{m}$ for both cases. We see the experimental conditions of Ref. [7] are above Ca_0, where our model shows the pure tank-treading motion as in Ref. [7]. The experimental conditions of Ref. [8] are below $\mathrm{Ca}_{\pi/2}$, where our model shows the swinging motion as in Ref. [8]. Thus, the present results can nicely explain the difference of two former experimental observations by Refs. [7,8], even without introducing any inertial effect. We also note that the phase transition during reorientation is observed for a prolate spheroidal capsule, although the results are not included here. Thus, the reorientation transition is robust regardless of the reference shape of the capsule.

The results obtained in this study illustrate that the reorientation transition appears in a wide variety of artificial and biological capsules. Given that the transition can be controlled by adjusting the background flow strength as well as the unsteadiness in the background flow direction, the results obtained here can be utilized for particle-alignment techniques in engineering applications, such as counting nonspherical particles by light scattering, making anisotropic materials, etc. These findings form a fundamental basis for the suspension mechanics of capsules and biological cells.

We are grateful for helpful discussions with D. Barthès-Biesel and A.-V. Salsac of Université de Technologie de Compiègne.

*omori@pfsl.mech.tohoku.ac.jp
†ishikawa@pfsl.mech.tohoku.ac.jp

[1] G. Jeffery, Proc. R. Soc. A **102**, 161 (1922).
[2] Z. Yu, N. Phan-Thien, and R. Tanner, Phys. Rev. E **76**, 026310 (2007).
[3] Y. Iso, D. Koch, and C. Cohen, J. Non-Newtonian Fluid Mech. **62**, 115 (1996).
[4] P. Bagchi and R. Kalluri, Phys. Rev. E **80**, 016307 (2009); D. Le and S. Wong, J. Comput. Phys. **230**, 3538 (2011); S. Kessler, R. Finken, and U. Seifert, J. Fluid Mech. **605**, 207

(2008); P. M. Vlahovska, Y.-N. Young, G. Danker, and C. Misbah, J. Fluid Mech. **678**, 221 (2011); J. M. Skotheim and T. W. Secomb, Phys. Rev. Lett. **98**, 078301 (2007); Y. Sui, Y. T. Chew, P. Roy, X. B. Chen, and H. T. Low, Phys. Rev. E **75**, 066301 (2007).

[5] S. Ramanujan and C. Pozrikidis, J. Fluid Mech. **361**, 117 (1998).

[6] J. Walter, A.-V. Salsac, and D. Barthès-Biesel, J. Fluid Mech. **676**, 318 (2011).

[7] T. Fischer, M. Stohr-Lissen, and H. Schmid-Schonbein, Science **202**, 894 (1978).

[8] M. Abkarian, M. Faivre, and A. Viallat, Phys. Rev. Lett. **98**, 188302 (2007).

[9] A. E. Green and J. E. Adkins, *Large Elastic Deformations* (Clarendon, Oxford, 1970), 2nd ed.

[10] R. Skalak, A. Tozeren, R. P. Zarda, and S. Chien, Biophys. J. **13**, 245 (1973).

[11] E. Foessel, J. Walter, A.-V. Salsac, and D. Barthès-Biesel, J. Fluid Mech. **672**, 477 (2011); T. Omori, T. Ishikawa, D. Barthès-Biesel, A.-V. Salsac, J. Walter, Y. Imai, and T. Yamaguchi, Phys. Rev. E **83**, 041918 (2011).

[12] See Supplemental Material at http://link.aps.org/supplemental/10.1103/PhysRevLett.108.138102 for movies.

[13] W. R. Dodson III and P. Dimitrakopoulos, Phys. Rev. Lett. **101**, 208102 (2008).

Eur Biophys J (2012) 41:571–578
DOI 10.1007/s00249-012-0811-y

BIOPHYSICS LETTER

EBSA
Biophysics in Europe

Blood oxygenation using microbubble suspensions

Noriaki Matsuki · Shingo Ichiba · Takuji Ishikawa · Osamu Nagano · Motohiro Takeda · Yoshihito Ujike · Takami Yamaguchi

Received: 24 November 2011 / Revised: 12 March 2012 / Accepted: 22 March 2012 / Published online: 3 April 2012
• European Biophysical Societies' Association 2012

Abstract Microbubbles have been used in a variety of fields and have unique properties, for example shrinking collapse, long lifetime, efficient gas solubility, a negatively charged surface, and the ability to produce free radicals. In medicine, microbubbles have been used mainly as diagnostic aids to scan various organs of the body, and they have recently been investigated for use in drug and gene delivery. However, there have been no reports of blood oxygenation by use of oxygen microbubble fluids without shell reagents. In this study, we demonstrated that nano or microbubbles can achieve oxygen supersaturation of fluids, and may be sufficiently small and safe for infusion into blood vessels. Although Po_2 increases in fluids resulting from use of microbubbles were inhibited by polar solvents, normal saline solution (NSS) was little affected. Thus, NSS is suitable for production of oxygen-rich fluid. In addition, oxygen microbubble NSS effectively improved hypoxic conditions in blood. Thus, use of oxygen microbubble (nanobubble) fluids is a potentially effective novel method for oxygenation of hypoxic tissues, for infection control, and for anticancer treatment.

Keywords Oxygenation • Microbubble • Nanobubble • Microbubble fluid • Fluid oxygenation

N. Matsuki (&)
Department of Biomedical Engineering, Graduate School of Engineering, Okayama University of Science, 1-1, Ridai-cho, Kita-ku, Okayama 700-0005, Japan
e-mail: nmatsuki@bme.ous.ac.jp

S. Ichiba • O. Nagano • Y. Ujike
Department of Emergency and Critical Care Medicine, Okayama University School of Medicine and Hospital, 2-5-1, Shikata-cho, Kita-ku, Okayama 700-8558, Japan

T. Ishikawa • T. Yamaguchi
Department of Bioengineering and Robotics, Graduate School of Engineering, Tohoku University, 6-6-01, Aoba, Aramaki, Aoba-ku, Sendai 980-8579, Japan

M. Takeda • T. Yamaguchi
Department of Bioengineering, Graduate School of Biomedical Engineering, Tohoku University, 6-6-01, Aoba, Aramaki, Aoba-ku, Sendai 980-8579, Japan

Introduction

Microbubbles are miniature gas bubbles, \50 Im in diameter, in liquids, which mostly contain oxygen or air (Kurup and Naik 2010; Qin et al. 2009). Microbubbles have been used in a variety of ways: in soil fermentation and hydroponic plant growth, in aquaculture, for environmental improvement of water and sewage treatment, and in engineering production. Microbubbles have several unique properties (Takahashi et al. 2003, 2005, 2007). They remain relatively stable in water for a long time (they have a long lifetime), or rise very slowly, gradual shrink, and finally collapse (i.e., shrinking collapse), whereas macrobubbles increase in size, rise rapidly, and burst at the water surface. The internal pressure of microbubbles is also much higher than that of the local environment, which accelerates dissolution of the gas into the liquid (i.e., efficient gas solubility). They also have a negatively charged surface, and thus will not merge to form larger bubbles, and the ability to produce free radicals, for example –OH.

The most beneficial property of microbubbles is the highly efficient gas solubility. The mechanism of supersaturation of oxygen gas in water is expressed by the Young–Laplace equation (Takahashi et al. 2007):

12 3

$$P \cdot P_l \cdot 2r = r$$

where P is the gas pressure, P_l is the liquid pressure, r is the surface tension of the liquid, and r is the bubble radius. Inertial gas pressure is higher for smaller bubbles, so the inertial pressure of shrinking microbubbles increases with decreasing size. According to Henry's law, the amount of dissolved gas around the shrinking bubble increases with increasing gas pressure. DP is defined as the inertial increase in gas pressure relative to environmental pressure:

$$DP \cdot 2r = r \cdot 4r = 2r \cdot 4r = D$$

where D is the bubble diameter.

For microbubbles 10 lm in diameter, the surface tension of water is 72.8 mN/m at 20 •C and DP is approximately 0.3 atm. However, when the microbubble diameter becomes 1 lm, DP increases tenfold (to approx. 3 atm).

Hypoxia, a condition of inadequate oxygen supply to tissues or the body, can lead to severe tissue damage and can be life threatening. Tissue hypoxia can develop if there is a decrease in cardiac output (ischemic hypoxia), hemoglobin concentration (anemic hypoxia), or oxygen saturation (hypoxic hypoxia), or an increase in the metabolic demands of the body (Abdelsalam and Cheifetz 2010). Hypoxia also induces physiological, cellular, and biochemical responses, which can effect pharmacological metabolism (Taylor and Moncada 2010; Ward et al. 2011, Donovan et al. 2010). Thus hypoxia is the most crucial issue in the treatment of a variety of diseases.

In medicine, microbubbles have been used as diagnostic aids to scan various organs of the body (Badea et al. 2009; Dijkmans et al. 2004; Lapotko 2011) and they have been studied for use in drug delivery and gene delivery (Dijkmans et al. 2004; Lapotko et al. 2011; Juffermans et al. 2004). There have recently been reports on use of microbubbles as local drug-delivery systems, using ultrasound with special shell reagents (Xu et al. 2011; Ferrara et al. 2009). However, biocompatibility of the shell reagents and ultrasound damage to the body are major problems that remain to be solved, as also is microbubble stability (Juffermans et al. 2006). Reports have also focused on special shell reagents for packing oxygen gas into microbubbles to extend the duration of oxygen delivery for injections (Cavalli et al. 2009; Swanson et al. 2010). In clinical applications of oxygen delivery to hypoxic patients, intravenous drip infusion is preferable because a large amount can be administered at once or over a long time.

Commonly used methods for generating microbubble suspensions are mechanical agitation, sonication, and pressurized gas–liquid mixing (microchannel emulsification); these usually result in the formation of microbubbles with wide size distributions. Gas–liquid mixing systems are preferable for generation of large amounts of microbubble suspensions at once, and bubble sizes are smaller. However, blood cannot be used directly in the machine because of blood cell destruction.

Therefore, methods for preparing fluids containing oxygen microbubbles (oxygen microbubble fluids) from conventional clinical fluids by use of gas–liquid mixing systems will be useful. There are no reports of blood oxygenation by use of oxygen microbubble fluids without shell reagents. This study was performed to determine:

- whether microbubbles could be used to efficiently increase the level of dissolved oxygen in liquids;
- how dissolved molecules such as electrolytes (e.g., NaCl) or glucose affect oxygenation of liquids; and
- whether oxygen microbubble fluid can improve oxygenation of hypoxic blood.

We found that normal saline solution (NSS) containing oxygen microbubbles (OMNSS) improves hypoxic conditions in blood.

Methods

Liquid solutions and blood samples

Sodium chloride and glucose (Wako Pure Chemical Industries, Osaka, Japan) were dissolved in ultrapure water as 1–10 % and 5–20 % solutions, respectively.

Approximately 100 ml blood was collected in a blood bag for autologous blood transfusion (Terumo CPDA blood bag, 200 ml; Terumo, Tokyo, Japan), from the ear vein of a healthy swine under general anesthesia, and stored in a refrigerator at 4 •C for 4 weeks. Each blood sample was taken from the blood bag by use of a disposable syringe (Terumo syringe, 2.5 ml; Terumo, Tokyo, Japan) to avoid contamination with air.

NSS (Otsuka Pharmaceutical, Tokyo, Japan) containing oxygen microbubbles was mixed with blood in dilution ratios of 10, 20, 30, 50 %. The samples were then gently shaken for 3 min before use in experiments.

These experiments were approved as animal experiment "no. 22-5" by the Ethics Review Committee for Animal Experimentation of Okayama University of Science.

Generation of microbubbles

Fine microbubbles of oxygen gas were generated by use of a micro-nanobubble aerator (AS-MA II; Asupu, Shizuoka, Japan), with hydrodynamic function, for 15 min, during which time oxygen gas was supplied at 1 l/min (Fig. 1). In the apparatus, water or another liquid (150 ml), introduced by a pump, spirals up along a wall and down to an outlet along the center of the apparatus. The centrifugal force

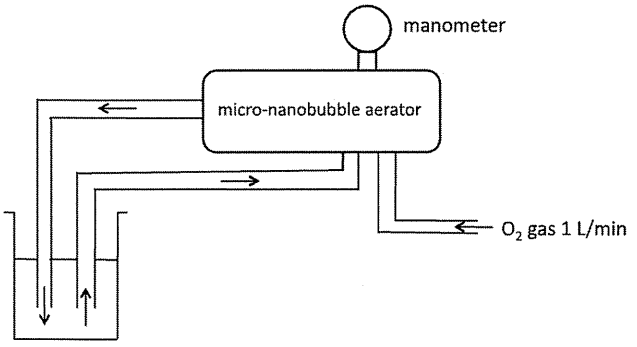

Fig. 1 Experimental setup. Relatively fine microbubbles of oxygen gas were generated by use of a micro-nanobubble aerator, at a peak pressure of 1–1.5 MPa, through which water or another liquid (150 ml) was circulating, for 15 min, and to which oxygen gas was supplied at 1 l/min. Fine microbubbles of oxygen gas were generated after brief sonication

caused by the circulation automatically introduces oxygen gas from the gas inlet and a vortex of oxygen gas is formed along the central axis. The body of the oxygen gas is separated into fine bubbles at the outlet of the apparatus by the strong shearing force of the dispersed water/liquid and circulation power. After generating water/liquid with oxygen gas microbubbles, the fluid was exposed to an ultrasonic bath (AUC-1L; As One, Osaka, Japan) for a few seconds to eliminate relatively large microbubbles.

For comparison purposes, macrobubbles were generated by use of an aquarium air stone (Round Air Stone S-2S; Daiko, Nagoya, Japan), to which oxygen gas was supplied at 1 l/min.

Morphological analysis of oxygen microbubbles generated in liquid

After brief sonication each 10 lm of the ultrapure water containing oxygen microbubbles was immediately mounted on a dual chamber slide (TC10™ System Sample Slides; Bio-Rad, Hercules, CA, USA). The oxygen microbubbles were then captured by microscopy (BZ-8100; Keyence, Tokyo, Japan), morphologically analyzed, and the bubble sizes measured.

Evaluation of dissolved oxygen in liquid or blood samples

After application of brief sonication, each fluid containing oxygen microbubbles was left for 30 s. The dissolved oxygen partial pressure (Po_2) in each liquid and blood sample mixed gently with NSS containing oxygen microbubbles for 3 min was then immediately measured, as an index of oxygenation, by use of a blood gas analyzer (ABL510; Radiometer, Copenhagen, Denmark). Each sample was taken by use of a disposable syringe to avoid contamination with air at room temperature (25 •C).

Statistical analysis

Results from the experiments are shown as the mean ± standard error of the mean (SEM). Statistical analysis was performed using StatMate III software (ATMS, Tokyo, Japan). Means were compared by use of unpaired t tests, or by analysis of variance (ANOVA) and Tukey's post-hoc test. In all analyses, P \ 0.05 was taken as indicative of statistical significance.

Results

Generation of microbubbles

To confirm the generation of fine microbubbles by the micro-nanobubble aerator, ultrapure water containing fine oxygen microbubbles was morphologically analyzed by microscopy.

Figure 2a shows the distribution of oxygen microbubbles in ultrapure water after circulation through the micro-nanobubble aerator—96.2 % of the generated oxygen bubbles were less than 50 lm in diameter (microbubble). Most (35.7 %) microbubbles were 20–30 lm in diameter, and a significant amount (26.2 %) of relatively fine microbubbles less than 20 lm in diameter was also present.

Figure 2b shows the fine oxygen microbubbles generated after brief sonication. Bubbles were less than 10 lm in diameter and inhomogeneous (ranging from \1 to 6 lm in diameter). Some fine microbubbles were seen to shrink and collapse during morphological analysis.

Evaluation of dissolved oxygen in liquids containing macrobubbles and microbubbles

To examine the potency of microbubbles for dissolving oxygen gas in liquid, the Po_2 in ultrapure water was compared between macrobubbles (f [1 mm) and microbubbles by blood gas analysis. Figure 3 shows the Po_2 values in ultrapure water. Means were compared by ANOVA and Tukey's post-hoc test. On average, oxygen gas was dissolved with Po_2 of 170 ± 5.6 mmHg (mean ± SEM) in the control (P \ 0.01 vs. macro and microbubbles), 776.8 ± 19.3 mmHg in ultrapure water exposed to oxygen macrobubbles (P \ 0.01 vs. control and microbubbles), and 1,003.2 ± 25.5 mmHg in ultrapure water containing oxygen microbubbles (P \ 0.01 vs. control and macrobubbles). These results suggest that oxygen microbubbles could significantly increase the Po_2 values in ultrapure water compared with macrobubbles.